RSC Advances

PAPER

View Article Online
View Journal | View Issue

Cite this: *RSC Adv.*, 2025, **15**, 27531

Unlocking porosity: structural tuning of urea-based MOFs *via* reaction parameter control†

Leili Esrafili, [a] Ocean Cheung, [b] Peter Adriaensens, [c] Elien Derveaux, [c] Lawson T. Glasby, [d] Peyman Z. Moghadam [e] and Christophe M. L. Vande Velde *[a]

In the synthesis of metal–organic frameworks (MOFs), efforts to increase the pore sizes by elongating linkers often result in interpenetration, a challenge that is exacerbated when functional groups are added. Urea groups and their derivatives play an important role in supramolecular chemistry by providing directional hydrogen bonding donor sites and are often considered "privileged groups". Incorporating these moieties into MOFs allows for their spatial separation, a critical approach to enhancing their functional activity, simultaneously preventing interpenetration, and enlarging the pore size. In this study, we synthesized hydrophilic urea-functionalized MOFs using zinc ions and the ligands 4,4′-(carbonylbis(azanediyl))dibenzoic acid (L1) and 1,3-di(pyridin-4-yl)urea (L2). Different levels of interpenetration and pore size were produced by varying temperature and starting material concentrations. UA-1 and UA-2 displayed 4-fold interpenetration. Notably, UA-3 formed non-interpenetrated 1D hexagonal mesoporous channels with six urea groups around each hexagonal pore, making it the first example of a non-interpenetrated mesoporous urea MOF. This topology differs from existing RCSR representations. We also investigated the host–guest interactions when introducing various organic molecules into UA-3, using a combination of single crystal X-ray diffraction (SCXRD), thermogravimetric analysis (TGA) and solid-state nuclear magnetic resonance (ss-NMR) spectroscopy. SCXRD provided insight into the amount and position of solvent molecules within the channels of the framework.

Received 15th April 2025
Accepted 22nd July 2025

DOI: 10.1039/d5ra02649k

rsc.li/rsc-advances

1. Introduction

The emergence of metal–organic frameworks (MOFs) has gained enormous attention in the field of coordination chemistry and materials science over the past two decades, because of their unique properties such as tunability,[1] permanent porosity, and defined reaction environments,[2] which allow them to be used in a wide range of applications.[3–5] Hydrogen bond donors can act as effective Lewis acid catalysts inside biological systems, playing a pivotal role in many enzyme-driven reactions.[6] Incorporation of hydrogen-bond-donating (HBD) moieties into various platforms like polymers offers biomimetic functionality and has emerged as a promising substitute to conventional Lewis acid activation.[7,8] However, in homogeneous systems, the effectiveness of HBD groups is often limited due to self-association (*e.g.*, dimer or oligomer formation), which diminishes their functional accessibility.[9,10] To address this obstacle, there is considerable potential to explore new avenues and opportunities by incorporating HBD moieties into coordination polymers. These polymers can create defined reaction environments (which due to their crystallinity can be studied easily) and maintain high porosity, thereby preventing the self-assembly and self-quenching of the HBD units.[11,12] HBD groups as catalysts help orient the substrate, reduce the activation energy for reactions, and play a role in determining the enantiomeric excess of the products.[13] Simultaneously, the increasing focus on biomimetic technologies worldwide raises an important challenge: designing artificial enzymes and molecules that can match the performance of those found in nature with improved economy and stability. This pursuit demands the collaborative expertise of chemists and material

[a]*iPRACS, Faculty of Applied Engineering, University of Antwerp, Groenenborgerlaan 171, 2020 Antwerpen, Belgium. E-mail: christophe.vandevelde@uantwerpen.be*

[b]*Nanotechnology and Functional Materials, Department of Materials Science and Engineering, Uppsala University, SE75121, Sweden*

[c]*Analytical and Circular Chemistry (ACC), NMR Group, Institute for Materials Research (imo-imomec), Hasselt University, Agoralaan, Diepenbeek, 3590, Belgium*

[d]*The Department of Chemical and Biological Engineering, The University of Sheffield, Sheffield, S10 2TN, UK*

[e]*Department of Chemical Engineering, University College London, London, WC1E 7JE, UK*

† Electronic supplementary information (ESI) available: The X-ray crystallographic data for UA-1,2 &3, UA-3-Ex-NM, UA-3-Ex-DIM, UA-3-Ex-N, UA-3-Dry, UA-3-Dry-NM, UA-3-Dry-DIM, UA-3-Dry-NS has been deposited at the CCDC as supplementary data with deposition number of: 2389779, 2389772, 2389773, 2389776, 2389778, 2389777, 2389774, 2389770, 2389775 and 2389771. For ESI and crystallographic data in CIF or other electronic format see DOI: https://doi.org/10.1039/d5ra02649k

scientists, spanning fields from pharmaceuticals to essential synthetic transformations.[14–16]

The first work on integrating hydrogen-bond donor (HBD) groups, which are recognized for their ability to self-assemble and hence self-quench, into a MOF backbone was conceived and performed by Farha, Hupp, Scheidt, and their collaborators.[17–19] Despite this progress, the immobilization of HBD groups within MOF scaffolds has suffered setbacks, mainly due to the small pore size and the unpredictable nature of the structures.[20,21] The primary objective in developing MOF-based catalysts is to maximize the volume of a single channel and construct a material with the lowest density, while maintaining sufficient rigidity to endure the removal of solvent molecules used during synthesis.[22] Simultaneously, these catalysts need to integrate functional groups that are crucial for enabling reactions. A simple approach to expand the cavities or channels in a MOF of a given topology is to increase the length of the rigid organic linkers while keeping the coupling units, or secondary building units (SBUs), unchanged.[23–26] However, this strategy presents a significant challenge: the highly porous nature of MOFs means that when the voids grow too large, both the SBUs and linkers, along with guest molecules, may occupy the pores, possibly resulting in additional networks forming within the structure. The formation of interpenetrating networks substantially decreases the pore volume, thereby restricting the space within the MOF. Functional groups present in the linkers play an important role, because they can develop specific chemical interactions with metal ions or other linkers, driving the entanglement and interlocking processes in the MOF.[27] Non-covalent interactions, including hydrogen bonds, π–π stacking, and van der Waals forces between functional groups on different linkers, help stabilize these interlocked structures, promoting interpenetration. Controlling this interpenetration is critical since it affects the pore dimensions and chemical environment, the diffusion properties of guest molecules, and the overall stability of the structure.[28] It is challenging to avoid interpenetration for certain combinations of SBUs and linkers, but it can occasionally be accomplished by carefully adjusting solvothermal reaction conditions. Some effective techniques involve using alternative solvents, integrating removable templates, or changing the ratios of linkers and SBUs.[29,30] A prevailing hypothesis in MOF chemistry suggests that interpenetrating networks enhance stability, particularly under high temperatures and concentrations, which promote increased interpenetration. This article, however, examines a case where this assumption does not hold.[31,32]

The tunable porosity of MOFs combined with their ability to maintain active HBD groups facilitates fast mass transport and interactions with substrates. These advantages, often difficult to achieve in homogeneous systems, set MOFs apart from other porous materials. Moreover, among the plethora of MOF-based catalysts, hydrogen-bonding organocatalysts have met MOFs only recently.[33] Urea, thiourea, pyrrole and squaramide moieties represent the most common hydrogen-bond donors used for the preparation of these MOF catalysts. To develop useful and efficient heterogeneous catalysts, MOF-derived HBD catalysts must be designed with essential properties including large accessible pores or channels to accommodate and selectively interact with differently sized substrates, and chemical stability to remain active. In addition to catalysis mentioned structural and functional properties are highly desirable for separation and sensing applications. The presence of directional H-bond donor groups can enhance selectivity for polar analytes or guests with hydrogen-bond acceptors like oxoanions.[34,35]

From a topological viewpoint, preventing interpenetration in MOFs is particularly difficult due to the translational symmetry inherent in different networks, which makes them equivalent within the bulk structure. This study addresses that challenge by synthesizing three novel topologically isomeric MOFs that incorporate urea functionalities—an area that remains underexplored due to the complexities that functional groups add to the synthesis process. Building on insights from our previous research with TMU-31,[36] we carefully adjusted temperatures and starting material concentrations. While TMU-31 demonstrated a diamantoid structure with an eight-fold interpenetrating framework, we will demonstrate that UA-1 and UA-2 feature four-fold interpenetrating networks, and that, remarkably, compound UA-3 crystallizes as a highly desirable structure with non-interpenetrated, one-dimensional mesoporous hexagonal channels. The comprehensive analysis of UA-3, utilizing various topological assignment tools including ToposPro and CrystalNets, will reveal a novel topology. The unique combination of large, uniform hexagonal channels and a dense array of hydrogen-bond donor groups makes UA-3 a promising candidate for future studies in applications like molecular separation, chemical sensing and heterogeneous hydrogen-bond catalysis. To further investigate the capabilities of UA-3, we will examine host–guest interactions between various organic components and the MOF pores. The arrangement and accessibility of the urea groups in the non-interpenetrated framework we will demonstrate, should create an excellent platform for selective adsorption and catalysis.

2. Experimental

All solvents and reagents were purchased from commercial suppliers and used without further purification. The synthesis of the organic linkers L1 (4,4′-(carbonylbis(azanediyl))dibenzoic acid) and L2 (1,3-di(pyridin-4-yl)urea), as well as full details of the instrumentation used (including SCXRD, PXRD, TGA, gas sorption, and solid-state NMR), are provided in the ESI.†

2.1 General synthesis procedure

The synthesis involved identical starting materials but varied concentrations of $Zn(NO_3)_2 \cdot 6H_2O$ (M: metal node), L1 (4,4′-(carbonylbis(azanediyl))dibenzoic acid) and L2 (1,3-di(pyridin-4-yl)urea) linkers in equimolar amounts (1 : 1 : 1), dissolving them in *N*,*N*-diethylformamide (DEF). The reaction mixtures were then placed in glass vials and subjected to temperatures ranging from 80 °C to 120 °C for a duration of 3 days, followed by gradual cooling to room temperature over 48 hours.

Table 1 Effect of temperature and concentration on final UA-1, UA-2 and UA-3

L1 (mg)	L2 (mg)	M:$Zn(NO_3)_2 \cdot 6H_2O$ (mg)	Amount (mmol) of L1/L2/M (mmol)	DEF	Conc. Of L1/L2/M [M]	Temp (°C)	Crystal morphology
30	21.4	30 mg	0.1	10 ml	0.01	80	Plate(mon) + Rod(hex)
30	21.4	30 mg	0.1	10 ml	0.01	100	Oct(tet) + Rod (hex)
30	21.4	30 mg	0.1	10 ml	0.01	110	Rod(hex) + trace amount of Oct(tet)
30	21.4	30 mg	0.1	10 ml	0.01	120	Rod(hex)
30	21.4	30 mg	0.1	20 ml	0.005	80	Plate(mon)
30	21.4	30 mg	0.1	20 ml	0.005	100	Oct(tet)
3	2.14	3 mg	0.01	10 ml	0.001	80	Trace solids
3	2.14	3 mg	0.01	10 ml	0.001	100	Oct(tet)
300	214	300 mg	1	10 ml	0.1	120/110	Rod(hex)
300	214	300 mg	1	5 ml	0.2	120/110	Rod(hex)

Concentrations and conditions were varied as summarized in Table 1 (see Section 3.1).

2.2 Sample preparation for SCXRD

Colorless crystals of UA-1-Native, UA-2-Native, and UA-3-Native were directly isolated from the mother solution in DEF. These were used without further modification for single crystal X-ray diffraction (SCXRD) analysis. To prepare exchanged samples (UA-3-Ex-X), we soaked UA-3-Native crystals in separate vials containing different guest X solutions. Specifically, UA-3-Ex-NM was soaked in pure nitromethane (NM), UA-3-Ex-DIM in pure diiodomethane (DIM), and UA-3-Ex-NS in β-nitrostyrene (NS), dissolved in toluene.

2.3 Guest exchange and drying procedures

To study how guest molecules behave in dried samples (UA-3-Dry-X), first the UA-3-Native crystals were dried with a nitrogen stream flowing at 60 ml min^{-1}. Temperature was gradually raised by 20 °C per minute until it reached 250 °C and then held isothermally for 10 minutes to remove most of the residual solvent. At this stage, the crystals were soaked in the same guest solvents mentioned higher to create UA-3-Dry-NM, UA-3-Dry-NS, and UA-3-Dry-DIM samples. For solid-state NMR (ss-NMR) and TGA experiments, we followed a similar process but used molten NS at 65 °C instead of an NS solution in toluene, and subsequently washed the crystals with toluene.

3. Results and discussion

3.1 Synthesis and morphology control

To study the effect of reaction parameters on framework formation, we systematically varied the reaction temperature and concentration of starting materials while maintaining a constant molar ratio (1 : 1 : 1) of $Zn(NO_3)_2 \cdot 6H_2O$ (M), linker L1, and linker L2 in DEF. The details of the concentrations, temperatures, and resulting crystal morphologies are summarized in the table below.

With this approach, we were able to synthesize three unique structures which were distinct in topology and morphology: UA-1 (plate-like crystals with monoclinic symmetry), UA-2 (octahedral crystals with tetragonal symmetry), and UA-3 (rod-shaped crystals with hexagonal symmetry). It's worth noting that by adjusting the temperature and concentration of the starting materials, we could synthesize mixtures of different crystals together, as well as each structure in isolation. The most favourable outcome was consistently the robust rod structure of UA-3 (yield: 78%). Isolating UA-1 and UA-2 posed a challenge due to their formation at lower concentrations, resulting in limited yields of the final products (approximately 24% for UA-1 and 31% for UA-2). Fig. 1 shows the morphologies of the UA-1, 2&3 observed by optical and confocal laser scanning microscopy.

3.2 Structure characterization

Topological isomerism in functionalized networks can be significantly influenced by solvent molecules of different size and functionality. By deliberately altering the solvent from DMF to DEF, we successfully synthesized three novel MOFs derived from our previously reported TMU-31 structure with 8-fold interpenetration.[36] At high temperatures in a sealed system, the autogenous pressure increases, impacting the formation and the structure of the resulting MOFs. Studies indicate that higher reaction temperatures lead to MOFs with a greater coordination number of the central metal ion and increased dimensionality, while reducing the presence of coordinated solvent molecules.[32] However, our study yields opposite results. Through solvothermal reactions involving $Zn(NO_3)_2 \cdot 6H_2O$ and L1 and L2

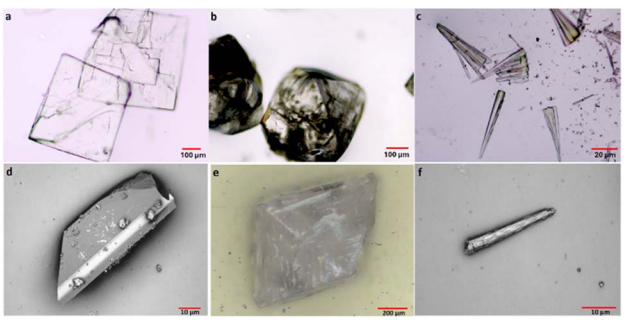

Fig. 1 Illustration of the different morphologies using optical (top) and confocal laser scanning microscope (bottom) for (a and d) UA-1 (b and e) UA-2 and (c and f) UA-3.

linkers in DEF solution at different temperatures, we obtained three distinct crystal morphologies UA-1, UA-2, and UA-3 (See Table 1.).

UA-1 (Zn(L1)(L2)) crystallized in the monoclinic space group $P2_1/n$ with unit cell parameters (at 100 K) of a: 18.5503(3), b: 14.3850(2) and c: 22.7569(4) Å and $\beta = 110.553(2)$. According to single crystal structure analysis, its asymmetric unit contains one Zn ion coordinated by two carboxylate oxygen atoms from L1 ligands and two nitrogen atoms from L2 linkers (Fig. 2a). The coordination geometry around Zn is distorted tetrahedral, common for Zn(II) with coordination number four. Within each coordination center, one of the oxygen atoms from the carboxylate group forms a hydrogen bond with a neighboring urea hydrogen atom. The other oxygen atom of the carboxylate groups forms a connection with the Zn atoms, contributing to the length of each rectangular unit. Each Zn(II) center can be considered a 4-connecting node, as it coordinates with four other Zn(II) atoms through the bridging ligands L1 and L2. Each L1 ligand serves as a rod-like unidentate tecton, linking two Zn(II) atoms and forming an infinite, corrugated one-dimensional (1D) chain. Simultaneously, N-donor L2 linkers bridge between these 1D chains, resulting in the formation of a three-dimensional (3D) structure. Two diethylformamide solvent molecules per asymmetric unit could be refined in the channel, the rest of the solvent content was calculated using the SQUEEZE algorithm within PLATON,[37] revealing that the pores contained a total average of 17.5 DEF molecules (8 explicit DEF, 9.5 "squeezed", for 608 additional electrons) per unit cell. UA-1 demonstrates a unique rectangular pore architecture with dimensions measuring 15 × 12 Å (Fig. 2b).

X-ray crystallography reveals that UA-2 (Zn(L1)(L2)) crystallizes in the tetragonal space group $P4_2/n$ with unit cell parameters of: $a = b$: 27.5833(3) and c: 14.4559(3) Å. (Cell dimensions and structure are measured at room temperature, as the tetragonal cell undergoes a transition to monoclinic at low temperature, and this leads to multiple twinning) In this compound, the coordination geometry around the Zn(II) can be described as distorted tetrahedral with the four coordination sites occupied by two oxygen atoms of carboxylate groups from two different L1 ligands and two pyridyl nitrogen atoms from two L2 ligands (Fig. 3a). The presence of the other carboxylate oxygen atoms severely distorts the tetrahedral coordination, but the bond distances to these oxygen atoms are much longer than could be expected for a Zn–O coordination bond. Each Zn(II) centre can be taken as a 4-connecting node being coordinated to

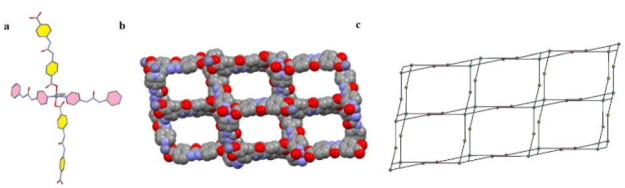

Fig. 2 (a) Representation of the coordination environment around Zn(II) for UA-1, (b) the space-filling model of the channel of UA-1 along the [010] direction (solvent removed) and (c) simplified view of the polycatenated array with dia; 4/6/c1; sqc6 topology for UA-1.

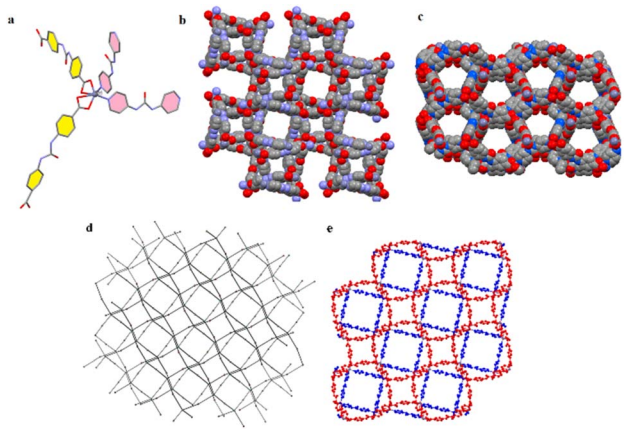

Fig. 3 (a) Representation of the coordination environment around Zn(II) in UA-2, three-dimensional structure along the (b) c and (c) a axis (d) simplified view of the polycatenated array with dia; 4/6/c1; sqc6 topology for UA-2, (e) orientation of L1 and L2 linkers within the 3D framework, L1 (red chain) and L2 (blue chain).

four other Zn(II) atoms through two L1 and two L2 bridging ligands. Upon closer inspection of the structure, it's apparent that one of the urea groups from an L1 linker forms a hydrogen bond with the carboxylic acid of another L1 linker, causing the first L1 linker to bend slightly. This arrangement creates square channels with diameters of about 17 and 7 Å along the crystallographic c axis (Fig. 3b). Fig. 3d illustrates the orientation of L1 and L2 linkers within these square channels. Moreover, along the crystallographic axes b and a, the structure shows pentagonal channels (Fig. 3c). The solvent content calculation from the SQUEEZE solvent mask showed that, on average, the pores contained 31.4 DEF molecules per unit cell (1761 electrons). Topological analysis using the TOPOS software indicates that UA-1 and UA-2 exhibit a 3D architecture with dia; 4/6/c1; sqc6 topologies (Fig. 2c and 3d).

The single-crystal X-ray diffraction analysis of UA-3 (Zn_2O(L1)(L2)) revealed a 3D non-interpenetrating structure crystallizing in the chiral space group $P6_422$ (or $P6_222$), with unit cell dimensions of: $a = b$: 32.2989(8) Å, c: 7.5643(19) Å. The asymmetric unit contains one Zn atom, half of an O atom, and half of the L1 and L2 ligands. Zinc atoms are linked into a coordination cluster, where each zinc centre is bridged to three neighbouring zinc atoms through oxygen atoms. Each zinc adopts a distorted tetrahedral geometry, coordinating with one nitrogen from L2, two carboxylate oxygen atoms from two distinct L1 ligands, and a single bridging oxygen atom. These zinc centres are connected *via* carboxylate bridges, forming 1D left- or right-handed helical SBUs. Two distinct types of channels were observed along the c-axis in the cross-sectional ab-plane: hexagonal 1D pores with a diameter of 2.8 nm, and smaller triangular pores measuring 1.2 nm. Inside each hexagonal channel, six urea groups are positioned, with N–H groups pointing inward, and carbonyl groups facing the triangular pores (Fig. 4). Solvent content calculations (*via* the SQUEEZE electron density) indicated an average of 15.25 DEF molecules per unit cell inside the pores (see also Table 3). Full

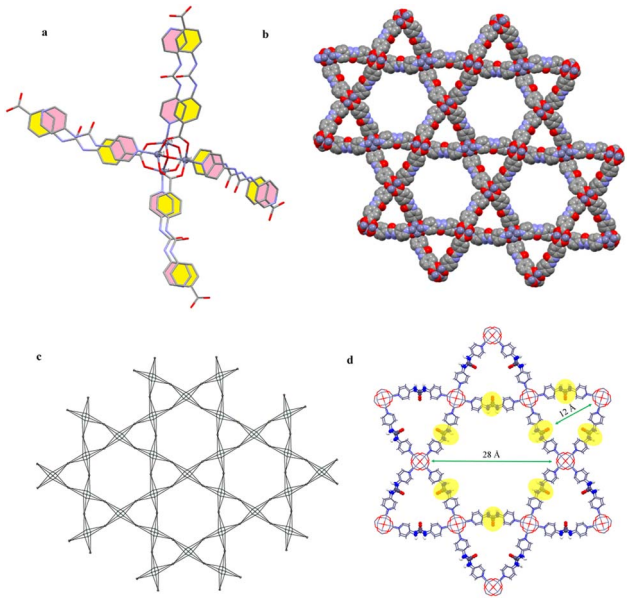

Fig. 4 (a) Representation of the coordination environment around Zn(II) in UA-3, (b) three-dimensional structure of UA-3, (c) simplified view of the polycatenated array with 43 c net topology for UA-3 and (d) orientation of urea functional groups inside pore channels highlighted in yellow.

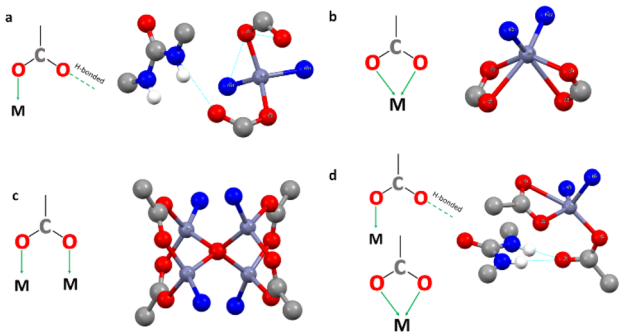

Fig. 5 Structural depiction of M-O-C units with carboxylate linkages coordinated to metal centres in various modes in (a) UA-1, (b) UA-2 (b), (c) UA-3, (d) TMU-31.

crystallographic data is presented in Tables S1 and S2 of the ESI,† the CIFs for the structures with solvent masks are available from the Cambridge Crystallographic Data Centre (CCDC) with deposition numbers: 2389779, 2389772, and 2389773 for UA-1, UA-2 and UA-3 respectively. The CIFs without solvent masks can be found in the ESI.†

All urea structures are assembled using the same linkers (L1&L2), but they differ in the type of link that connects the Zn–O–C units. In these units, there are tetrahedral and octahedral Zn(II) centers, respectively, bound to 4 and 2 carboxylate groups. In the case of UA-1 and TMU-31, two and one terminal carboxylate groups were observed to be hydrogen-bonded to the urea groups by one of the oxygen atoms. (N···H···OC, with distances of 2.81 Å for UA-1 and 2.98 Å for TMU-31). Strong hydrogen bonds among carboxylate groups and NH of urea groups result in oxygen groups preferring to engage in hydrogen bonding rather than bidentate oxygen-Zn interactions. In UA-2, coordination takes place through two chelating bidentate carboxyl groups. UA-3 coordinates to Zn with a μ-4 oxide ion bridging four Zn(II) atoms to form a tetranuclear $[Zn_4(COO)_4]$ SBU (Fig. 5). Unlike previous urea-functionalized MOFs, which often suffer from interpenetration and limited pore accessibility, UA-3 exhibits a non-interpenetrated structure with large, open hexagonal pores (2.8 nm) lined by six inward-facing urea groups. This arrangement provides an unusually high density of hydrogen-bond donors within a single pore environment.

Powder X-ray diffraction (PXRD) analysis was performed on UA-1, UA-2, and UA-3, which were ground into a fine powder for around 1 minute, using a ceramic mortar and pestle. The diffractograms of the as-synthesized UA-1 to UA-3 samples, are shown in Fig. S5–S7,† together with the powder pattern simulations based on the SCXRD structures.[38] The PXRD patterns for all materials closely matched their expected single-crystal phases, verifying the successful synthesis of each isolated structure. In cases of mixed-phase structures, the diffractograms displayed peaks from both materials. UA-3 demonstrated greater structural stability, making it the dominant isomer in mixed compositions. Strong characteristic peaks for UA-3 were observed at 2θ values of 3.19°, 5.5°, 6.4°, and 25.8°, corresponding to the parallel planes $(h, k, l) = (1\ 0\ 0)$, $(2\ -1\ 0)$, $(2\ 0\ 0)$, and $(4\ -1\ 2)$, respectively. The $(1\ 0\ 0)$ peak is particularly notable, being the primary indicator of the presence of UA-3 in mixed structures. Upon heating UA-3, the diffraction intensities for the $(1\ 0\ 0)$ and $(2\ -1\ 0)$ planes, located at 3.3° and 5.5° in 2θ, gradually decreased, with more prominent reductions at 250 °C. Diffraction peaks at lower angles provide information about the larger periodic features of the crystal structure. The first two peaks, in particular, reflect the periodicity from unit cell to unit cell, also of the disordered solvent in the pores. Losing solvent from the pores will affect these low order reflections very strongly (Fig. S7†).

Although the crystals, after heating and losing solvent, were still of sufficient quality for single crystal X-ray analysis, the diffraction patterns shows a strong decrease in the intensity, especially at higher angles. Consequently, the resolution and quality of the data sets decreased, the structural models suffered, and the overall R_1 factors increased. This is why, in further discussion of the dried and resolvated UA-3, results should be interpreted with care, as the underlying data are in some cases of insufficient quality.

Interpenetration is commonly observed in open-framework structures, where large voids within the material can become occupied by additional interwoven networks. Studies suggest that higher synthesis temperatures typically lead to greater interpenetration due to increased reaction kinetics, which accelerates crystal growth and raises the likelihood of network intertwining. Likewise, higher concentrations of starting materials are often linked to enhanced interpenetration. However, our study presents a different outcome. We observed that, despite using high concentrations of starting materials and elevated temperatures, the resulting structure was non-interpenetrated (Fig. 6). This outcome can be attributed to the

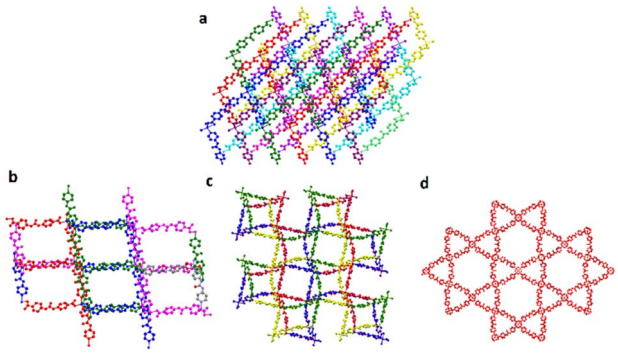

Fig. 6 Illustration showing interpenetration degrees: (a) TMU-31 (eightfold), (b) UA-1 (fourfold), (c) UA-2 (fourfold), and (d) non-interpenetrated.

inherent stability of UA-3 with hexagonal topology (Fig. S8†).[39] Hexagonal MOFs, characterized by densely packed structural units in one of the crystallographic axes, offer limited space for interpenetration without compromising the framework integrity, thus making interpenetration less probable than other topologies.

3.3 Topology studies of UA-3

Analysis of UA-3 in ToposPro,[40] using the standard representation method yields an unknown Reticular Chemistry Structure Resource (RCSR) result in a suggested 43 c net topology. However, using the cluster single node method with SBUs consisting of C4O9Zn4, we obtain the 8T780 TTD topology. Further analysis using CrystalNets[41] and single node clustering,[42] also produces an "unknown" topology result, revealing the underlying net shown in Fig. S1.† Here, while the pore network and shapes are clearly visible, we cannot directly match it with existing RCSR or EPINET entries.

UA-3 exhibits structural similarities in the '*c*' plane to NU-1000,[43] further analysis of NU-1000 using both Topos Pro and CrystalNets reveals an RCSR topology of csq, considering both all node and single node deconstruction techniques (Fig. S1†). However, when viewed from different planes ('*a*' or '*b*'), significant structural differences become apparent, the csq topology differs from 8T780 in the connectivity between these sheets. The 8T780 topology matches a similar structure in the CSD FUSYUO,[44] featuring large hexagonal pores and smaller triangular pores (Fig. S3†). Notably, structural differences arise depending on how the SBUs are considered. FUSYUO appears to feature two separate but bonded CdO polyhedral SBUs, creating interesting bonds between metal SBUs, linkers, and Cd metal atoms internally within the triangular pores. The reason for deviation from a standard csq representation is highlighted in Fig. S2.† If we consider each layer of the structure to be a 2D sheet bonded to another 2D sheet above and/or below *via* a linker, we can see the bonding between layers which should extend out from sheet to sheet to make the structure 3-periodic. In the case of UA-3, each sheet bonds to more than just its adjacent sheets.

To conclude, we report that 8T870 TTD is a good descriptor for UA-3, that it is not represented by the RCSR csq topology,[45] and additionally that an RCSR representation does not exist that would best describe the underlying net of this structure. Further to this, it is also unlikely that a sufficiently descriptive snet (EPINET) representation exists. Further details can be found in the ESI Material.†

3.4 Monitoring of the guest molecules uptake

The investigation of the interactions between guest molecules and the host framework, and the role of these guests in altering material properties, remains an understudied aspect of MOFs. Investigating pore chemistry involves introducing organic molecules with varying electron densities and functional groups into MOF channels. We examined two cases: native MOF containing DEF-filled pores and dry MOF with emptied pores. For the exchange series (UA-3-Ex-X), we immersed isolated UA-3-Native crystals in individual vials with nitromethane (NM), diiodomethane (DIM), and a 1 M solution of β-nitrostyrene (NS) in toluene. In the case of the "Dry" series of MOFs, we first dried the UA-3-Native crystals at 250 °C under nitrogen, then soaked them in the same guest solutions, producing UA-3-Dry-NM, UA-3-Dry-NS, and UA-3-Dry-DIM samples. This process allowed us to introduce various guest molecules into both native and dry MOFs.

Although PXRD is commonly used for structural characterization, it is not the most effective method for identifying confined guests. This limitation arises from two primary reasons: firstly, to contribute to the Bragg diffraction peaks, guests should exhibit long-range periodicity, which may not be the case as they are more likely to be disordered within the MOF host. Secondly, the weight percentage of confined guests, when compared to the MOF host, is typically low. Analyzing the structures using SCXRD instead, also necessitates considering several critical factors, like which part of the sample is no longer crystalline, as well as the rigorous treatment of disordered electron density.[46] Upon drying, the UA-3 crystals became opaque and lost their optical activity under polarized light. However, when the crystals were re-soaked in solvents, or even in the silicone oil used for mounting crystals, they gradually regained their transparency and optical activity, becoming responsive under polarized light once again. This change corresponds to the recovery of their crystalline structure during the guest molecule loading, making them suitable for further structural analysis. This conclusion is supported by ss-NMR results comparing both the dried and solvent-refilled MOFs.

Comparing the SCXRD structures of native and dried UA-3, the main difference is in the size and shape of the urea atomic displacement parameters, which become quite large and irregularly shaped, suggesting disorder or movement in the urea groups, especially in L1. An additional observation is that L1 shows quite a large shift away from the center of the large pore on drying, whereas L2 tends to move inward on the large pore, by a lesser amount. This has the effect that the stacking between the two different kinds of linkers becomes better in the dry MOF as opposed to the native one, and this change is not

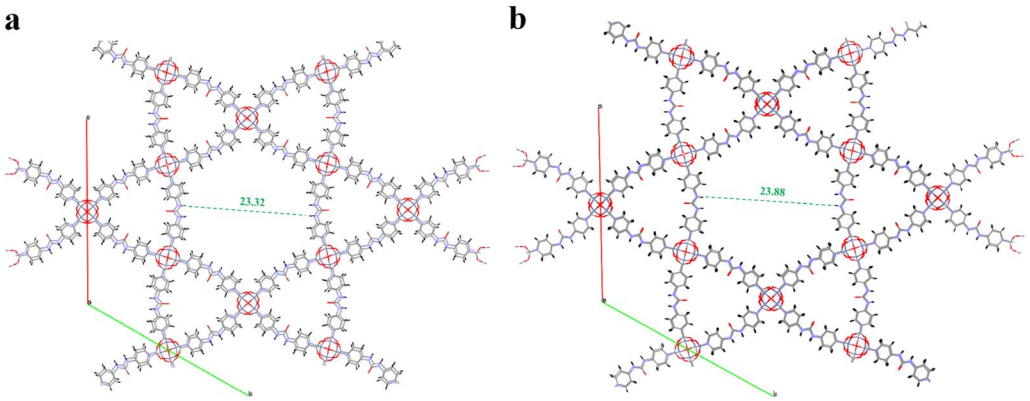

Fig. 7 Projections of the (a) native and (b) dry structures of UA-3 along the *c*-axis. Note the shift in the projection of the linkers – one of the diagonal N···N distances in Table 2 is indicated in the figures.

Table 2 Comparison of urea nitrogen distances across the large pore in UA-3-Native and UA-3-Dry

Urea nitrogen distance across the large pore	UA-3-Native	UA-3-Dry
L1–L1 (Å)	23.32	23.88
L2–L2 (Å)	24.47	24.36

undone when the dry MOF is refilled with a different solvent (see Fig. 7 and Table 2).

In order to retain sufficient crystallinity to be able to measure a single crystal diffraction pattern, the MOF could not be dried completely. It can be conceived that when all the hydrogen bond accepting solvent is removed from the pore, the urea moieties will shift, or even flip over, in order to hydrogen bond to other linkers in the stack, permanently destroying long-range order in the structure (and making it no longer amenable to single crystal diffraction).

Voids along the *c*-axis were filled with disordered solvent molecules. As the positions of these solvent molecules could not be clearly resolved on the Fourier maps, PLATON/SQUEEZE was employed to compensate for their contribution to the Bragg diffraction patterns. It should be remarked that for some of the dried and resolvated structures, the data on which these estimates of the electron densities are based are of low resolution and low quality. This may have an effect on the resulting numbers.

Two distinct pore sites were identified within UA-3, differing in shape, size, and presence of functional groups. After modelling the base MOF structure, and prior to applying the solvent mask, the remaining difference electron density hints at where the disordered guests are located. After applying a solvent mask to the structures, also the numbers of electrons removed from the model in the different voids suggest a number of guest molecules present. From these data (Table 3), it appears that more polar guests (*e.g.* incorporating nitro or amide groups), as expected, congregate around the hydrogen bond donors. Based on the examination of difference maps and electron density content, as modeled by the solvent mask,[37] it was determined that the native MOF contained 642 electrons in the hexagonal channels and 106 electrons in triangular channels, totaling 854 electrons. This finding suggests the potential presence of 15.25 DEF molecules/unit cell (at 56 electrons/DEF molecule) or 2.54 molecules of DEF per formula unit within the MOF structure. Consequently, it becomes feasible to predict the expected mass

Table 3 Comparative electron density and related parameters in small and large pores of UA-3

	Space group	R1	R1 after squeeze	e small cavity 1	e small cavity 2	e large cavity	e total	e/V	Fill fraction small cavity (fill rate)	Fill fraction large cavity (fill rate)	Fill fraction total (fill rate)
Native											
DEF	$P6_222$	7.88	3.55	106	106	642	854	0.242	0.83	0.76	0.78
UA-3-Dry.X(guest)											
Dry	$P6_222$	7.74	4.04	116	115	469	700	0.198	1.04	0.64	0.73
DIM	$P6_222$	17.62	10.5	140	141	702	983	0.278	0.39	0.29	0.32
NM	$P6_222$	14.84	8.06	131	131	794	1060	0.300	0.86	0.79	0.81
NS	$P6_222$	9.58	4.48	118	118	507	743	0.210	0.76	0.50	0.56
UA-3-Ex.X(guest)											
DIM	$P6_222$	9.4	2.8	140	139	703	982	0.278	0.39	0.30	0.32
NM	$P6_222$	6.68	2.14	120	120	594	834	0.236	0.79	0.59	0.64
NS	$P6_222$	7.5	4.3	106	106	628	840	0.238	0.68	0.62	0.63

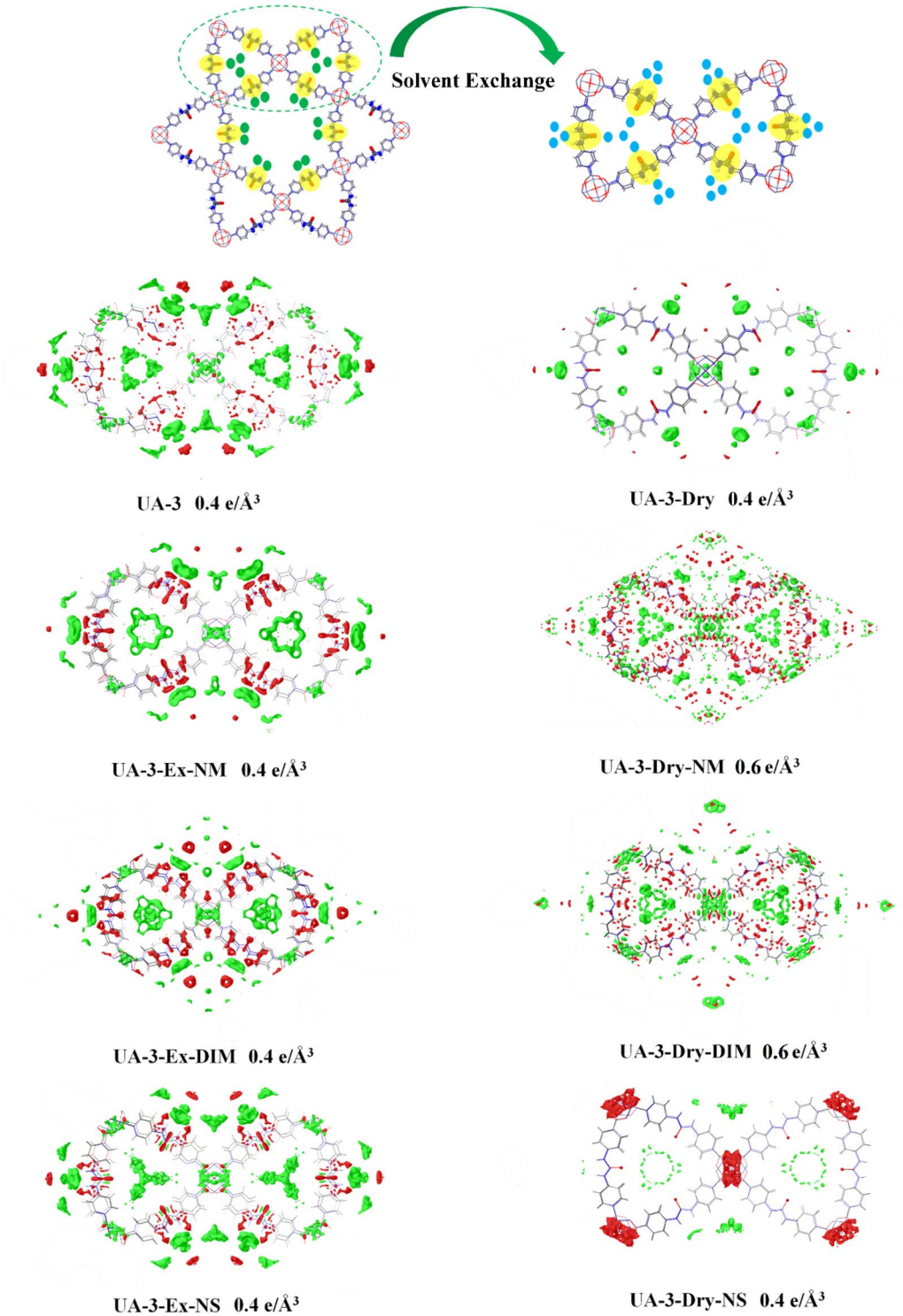

Fig. 8 Residual electron density maps of the structures without solvent mask: UA-3 native, Dry and UA-3-Ex/Dry.X(guest). The isosurface values of the positive (green) and negative (red) difference electron densities are indicated below the respective figures. For some of the "dry" structures, the isosurface levels have been chosen higher, due to the difference maps being quite noisy due to the inferior data quality yielded by the dried crystals.

loss if all solvent were to be expelled *via* thermal treatment. Additionally, it is apparent from the SCXRD structure of the dry MOF (after solvent removal at 250 °C for 20 minutes) that solvent persists within the crystalline pores, particularly in regions associated with the urea functionality, and to a higher degree than the weight loss by TGA (see further) suggests. The NM molecules demonstrated a higher fill rate in the dried MOFs compared to the exchanged MOF. In contrast, DIM yielded

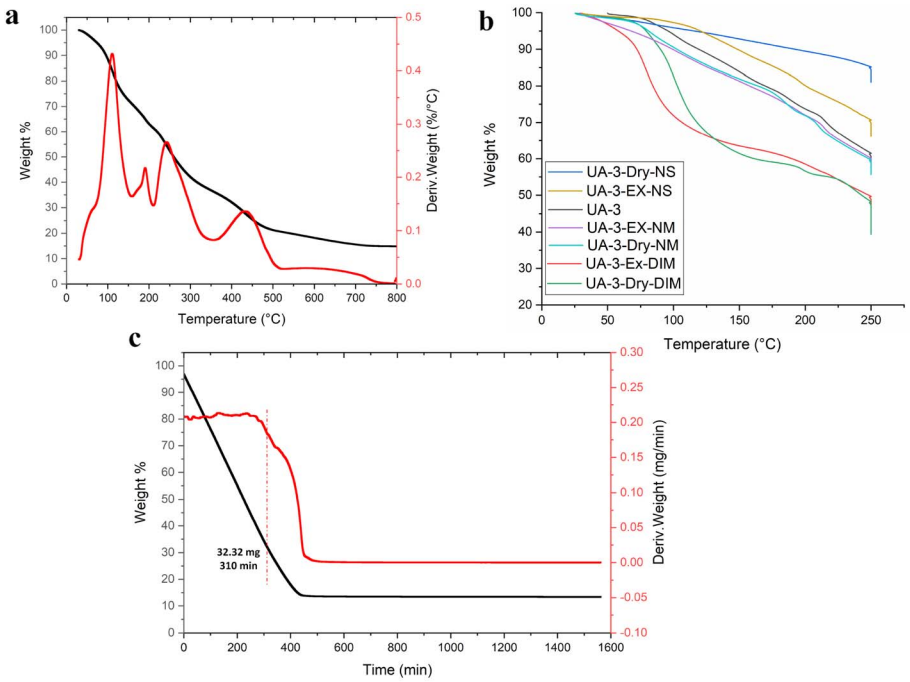

Fig. 9 Thermogravimetric analysis of (a) the as-prepared UA-3 at a heating rate of 10 °C min^{-1}, showing weight loss and temperature derivative of weight percentage *vs.* temperature (b) Normalized HR-TGA plots of UA-3 compared with UA-3-Ex-X & UA-3-Dry-X, (c) weight loss profile of UA-3-Dry refilled with DIM under N_2 at 23 °C, showing weight loss and the smoothed time derivative of weight percentage *vs.* time.

similar behaviour in both refilling and exchanging processes. Both dried and exchanged UA-3, after resoaking in DIM, displayed larger electron densities in the pores, consistent with the presence of heavier, more electron-rich DIM, compared to DEF. Specifically, UA-3-Dry-DIM displays 983 electrons in the pores, contrasting with 924 electrons in the same pores for UA-3-Ex-DIM (Table 3 & Fig. 8). Molecules containing hydrogen bond acceptors, such as NM, DEF, and in principle NS, should exhibit a notable affinity for regions linked to hydrogen-bonding urea groups within the MOF, as evidenced for NM and DEF by concentrations of residual density in the Fourier maps. This phenomenon is indicative of a strong interaction between these guest molecules and the urea functional groups, which plays a pivotal role in directing their distribution within the MOF structure. In contrast, DIM displays a preference for less polar sites, such as phenyl groups, the smaller triangular pores, or the center of the large pore.

3.5 TGA studies

Thermogravimetric analysis (TGA) was used to assess the thermal stability and solvent content of the UA-3 series of samples. The samples were heated in a nitrogen (N_2) atmosphere up to 800 °C at 10 °C min^{-1}. The TGA profile of UA-3-Native showed two weight loss steps between 25 and 210 °C, which we expect to correspond to the release of solvent molecules (DEF) accounting for approximately 38–40% of the total weight (approximately accounting for 25 molecules of DEF per unit cell) (Fig. 9a). The first weight loss step, observed at 110 °C, likely corresponds to the release of solvent molecules from the centre of pores, accounting for approximately 31% of the total weight. The second weight loss step occurs at 190 °C and contributes about 10% of the total weight. This step is presumably associated with the removal of DEF molecules that are strongly bound to functional groups within the pores. The third step, observed at 240 °C, corresponds to the onset of decomposition of the MOF framework. At this point, the long range order of the structure is significantly impacted. The remaining residue at 800 °C (14.5%) likely consists of ZnO (Fig. 9a). When the samples were held at 250 °C‡ for 20 to 60 minutes under N_2, the total weight loss ranged from 38–40% (Fig. S11†), corresponding to the first two steps mentioned higher. The remaining ZnO of UA-3-Native after TGA under air atmosphere was measured to be 14.37% of the total weight (Fig. S12b†). This corresponds to the expected, calculated amount of ZnO, if an initial solvent content of 40% (25,75 molecules of DEF per unit cell) is assumed. The persistent presence of DEF in the crystalline material (as evident in SCXRD) suggests strong interactions between the solvent molecules and the functional groups within the MOF, making complete solvent removal challenging without damage to the structure. In the samples where single crystal diffraction patterns could still be recorded from the dried structure, some remaining DEF was also observed in the pores (see Tables 3 and 4). From the electron density of the solvent mask (Tables 3 and 4) we found a total number of 15.25 DEF molecules in the native MOF, and 12.50 DEF molecules in dried UA-3.

‡ There is also some dependence of the desolvation and decomposition temperature on the crystal size of the sample.

Table 4 Weight loss percentage, solvent content, and comparison of the expected number of electrons calculated from TGA weight loss, and calculated numbers of electrons from the SCXRD solvent mask for UA-3, UA-3-Ex-X, and UA-3-Dry-X (per unit cell)

MOFs	UA-3	UA-3-Ex-DIM	UA-3-Dry-DIM	UA-3-Ex-NM	UA-3-Dry-NM	UA-3-Ex-NS	UA-3-Dry-NS
Weight loss%	40%	56%	61%	41%	43%	34%	19%
No. of solvent molecules from TGA weight loss	25.7	18.5	22.7	45.2	49	13.5	6.1
No. of electrons expected from TGA weight loss	1442	2111	2594	1445	1569	1038	473
No. of electrons from solvent mask (SCXRD)	854	922	983	834	1060	840	743

High-resolution TGA curves of UA-3-Ex-X and UA-3-Dry-X (Fig. 9b) reveal distinct weight loss behaviours based on the type of solvent present within the MOF structure. All TGA curves were normalized to allow accurate comparison of solvent retention across samples with different evaporation rates. The extent of weight loss varies notably with the solvent type, with UA-3-Dry-DIM showing the greatest reduction (~61%), followed closely by UA-3-Ex-DIM at 56%, which corresponds to approximately 22 and 28 DIM molecules per unit cell respectively. These values are in close agreement with the theoretical solvent content, estimated based on the density of liquid DIM in the empty pore volume. The considerable weight loss observed for DIM can be attributed to its higher density and molecular weight relative to the other solvents used. The slightly lower weight loss observed for the "Ex" sample (56%) can be due to strongly bound DEF not having been exchanged. UA-3-Native was also dried to remove the DEF and subsequently refilled with DIM twice, to study the isothermal release profile. The sample was placed in the TGA at 23 °C under an N_2 stream for approximately 24 hours to monitor weight loss. This experiment aimed to clarify the origin of the initial weight loss observed during the TGA runs at a temperature gradient. The weight loss profile, shown in Fig. 9c, demonstrates a stable evaporation rate of excess liquid DIM until a slight change in the slope of the curve occurs (at 32.3 mg, UA-3 dry weight 12.4 mg), indicating the end of evaporation of excess liquid DIM on the outside of the crystals, and the beginning of DIM release from the pore network. Taking this point at 32.3 mg as 100%, this means 61.6% of the total weight is DIM, consistent with the density of liquid DIM and the pore volume in the crystal from SCXRD, which would yield 63.78% DIM retention. The amount of DIM resulting from the electron density of the solvent mask in the SCXRD refinement would correspond to 8.6 molecules of DIM, and a presumed 37% of the total weight – this is clearly the less accurate figure. After 24 h at 23 °C there is still approximately 0.84 mg of DIM present trapped within the pores, which is only released upon heating (Fig. S12a†). Further heating in air atmosphere leads to the complete release of DIM, and the decomposition of the structure, leaving residual ZnO that amounts to the expected 24% of the dry mass of UA-3 as the final product.

The weight losses observed for UA-3-Dry-NM and UA-3-Ex-NM are approximately 43% and 41%, respectively, corresponding to an estimated 49 and 45 NM molecules per unit cell. These values do not fully align with the theoretical solvent content expected for complete pore filling with liquid NM. The discrepancy originates on the one hand from crystals not being entirely dry, with a small amount of liquid NM still present on the surface, which is released in the TGA around 25 °C. On the other hand, NM is also more likely to form strong hydrogen bonds with the urea functional groups, leading to a density of NM within the pore that is higher than the density of liquid NM. This is also the case for DEF.

For UA-3-Ex-NS, the weight loss is only about 34%, while UA-3-Dry-NS exhibits the lowest loss at 19%. These results suggest that NS has some difficulty filling the empty pore entirely, and that in the NS exchange sample, part of the weight loss is due to the DEF molecules still within the pores. The electron density data from SCXRD was determined with samples exchanged with a toluene solution of NS for reasons of crystal quality, which makes the comparison with the TGA results (exchanged with molten NS and washed with toluene) strenuous. Nevertheless, the NS-exchanged samples exhibit the lowest electron densities in the series of samples.

3.6 Porosity analyses by gas adsorption

N_2 sorption experiments were carried out at −196 °C to investigate the porosity of UA-3. As UA-3 becomes amorphous after complete drying, it was first activated by supercritical CO_2 and then at 200 °C under a slow flow (5 ml min^{-1}) of N_2. The N_2 adsorption/desorption isotherms in Fig. S13† show that UA-3 contains a majority of micropores (type I isotherm). The pore size distribution of the micropores in UA-3 was calculated using DFT with a slit pore model (Fig. S15†). A significant amount of micropores between 1-2 nm was observed according to the modelled isotherm data. In addition, the desorption isotherm shows a stepwise hysteresis that indicates the notable presence of mesopores as well as the micropores discussed above. Indeed, the BJH desorption pore size distribution (Fig. S14†) shows that UA-3 contains mesopores of approximately 3.8 nm in size. Note that the pore sizes calculated using sorption data may not agree fully with the crystallographic pore size (1.2 nm and 2.8 nm) due to flexibility of the framework as well as other dynamic effects. The specific surface area of UA-3 calculated using the Brunauer–Emmett–Teller (BET) model, was ~497 m^2 g^{-1} with a total pore volume of 0.25 cm^3 g^{-1} ($p/p^0 = 0.98$). The calculated pore volume from SCXRD for the solvent-free UA-3 corresponds to 0.492 cm^3 g^{-1}. This was corroborated by the

isothermal TGA measurement with DIM described higher, where 20.3 mg of DIM could be adsorbed to 12.4 mg of dry UA-3, which, by assuming the density of liquid DIM for the density of the solvent adsorbed in the pores, corresponds to 0.483 $cm^3\ g^{-1}$. This suggests that despite using supercritical CO_2 to evacuate the pores, either they were not emptied completely, or the structure has partially collapsed. Additional gas adsorption isotherms were recorded at 20 °C with CO_2, CH_4 and SF_6 as probe gases and these isotherms are presented in the ESI (Fig. S16†).

3.7 Solid state ^{13}C-CPMAS NMR studies

ss-NMR is a powerful technique to study the chemical structure, composition, dynamics and organization of materials.[47] In this study, it is used to gain detailed insights into the dynamics of guest molecules within MOFs and serves as a sensitive probe for short-range structure and crystallinity. This capability makes ss-NMR an excellent complement to single-crystal X-ray diffraction and TGA data. Notably, the adsorption of guest molecules does not significantly disrupt the long-range order of the crystal lattice, as indicated by the largely unchanged powder XRD patterns observed before and after guest exchange.

Spectral analysis was conducted on eight different samples - UA-3-Native, UA-3-Dry, UA-3-Ex-X, and UA-3-Dry-X with X = NM, DIM and NS, using solid-state ^{13}C-CPMAS NMR to probe the local chemical environments. For UA-3-Native, peaks corresponding to DEF were observed at 13–15 ppm and 37–43 ppm, originating from the methyl and methylene carbons of DEF (ethyl group), as well as a peak at 164 ppm attributed to the C=O group of DEF, and a small signal at 170 ppm which we attribute to DEF directly hydrogen bonded to urea (see below). Peaks from the aromatic carbons and urea C=O groups in the L1 and L2 ligands were detected between 110–155 ppm, and the COOH carbons from L1 were observed at 174 ppm (Fig. 10a). Following thermal treatment of UA-3-Native to produce UA-3-Dry, notable changes were observed in the ^{13}C-NMR spectrum. The peaks of UA-3-Dry became broader, reflecting a less ordered structure and reduced crystallinity due to the removal of DEF during the thermal process (Fig. 10a). However, the DEF-related ethyl signals persisted in small amounts, indicating incomplete solvent removal. Additionally, the carbonyl signal at 170 ppm, which we conclude is likely associated with the DEF carbonyl group bonded to the urea groups in the framework, persists as well. This incomplete removal suggests that DEF plays a crucial role in maintaining the structure and order of the MOF framework.

When the UA-3-Dry crystals were resoaked in NM, a notable improvement in crystallinity was observed compared to the dry MOF. The appearance of a new peak at 63 ppm in the UA-3-Dry-NM spectrum is attributed to the methyl carbon of NM. In contrast, when UA-3-Dry crystals were soaked in DIM, only a modest improvement in crystallinity was observed, as well as a new peak at −64 ppm associated with the methylene carbon of DIM. It is important to note that the −64 ppm DIM signal partially overlaps with a spinning sideband due to the 17 kHz rotor spinning rate used in this study, as demonstrated in spectra acquired at lower spinning rates of 13 and 15 kHz (Fig. S17†), in which the −64 ppm signal persists. No significant improvement in crystallinity was observed for UA-3-Dry-NS samples, which were soaked in molten NS and stirred at 65 °C for 2 hours, then washed with toluene. However, small peaks related to NS were evident at 90 ppm and 130 ppm, indicating the presence of NS within the MOF, despite the limited improvement in overall crystallinity. To further evaluate the impact of guest exchange, DEF in UA-3-Native was replaced with NM, DIM, and NS. The replacement of DEF with NM was confirmed by the appearance of a new peak at 63 ppm for the methyl carbon of NM and the nearly complete absence of DEF ethyl signals at 13–15 ppm and 37–43 ppm. Despite this, the upfield shoulder near the COOH peak at 170 ppm could still be observed and indicated that all remaining DEF molecules within the framework are likely associated with the urea NH groups. Residual DEF was more pronounced in DIM- and NS-exchanged samples, suggesting that the efficiency of guest exchange and DEF removal varies depending on the guest molecule used (Fig. 10b and c).

In the case of UA-3-Ex-NM, a shift of resonance signals associated with phenyl groups (110–160 ppm) was observed, mainly moving to lower chemical shifts after NM exchange. This shift is more pronounced for NM than for DIM and NS, suggesting that the interaction between the guest molecule and the framework is strongest in the NM-soaked sample (Fig. S18†). The observed shifts can be attributed to hydrogen bonding interactions between the nitro groups of NM molecules and the urea NH groups, which influences the shielding of the phenyl groups. Since the effect observed is more pronounced for the aromatic peaks in the 140–155 ppm range, we can infer from comparison with the SCXRD data, where we see larger Fourier peaks around the L2 urea group (Fig. S19†) that these signals are primarily associated with the L2 ligand. The interaction explains why these peaks experience a greater shift compared to the peaks between 110–135 ppm, which are in general less affected. Overall, these ss-NMR results, along with the SCXRD data (Fig. S19†), indicate that while guest removal and replacement influence the crystallinity of the MOF, the framework's long-range order remains largely preserved. We thus assume that on full removal of all hydrogen bonded guests, the "free" urea moieties reorient to try to H-bond to each other, for lack of other hydrogen bond acceptors, destroying a particular aspect of the long range order in the process. The extent of

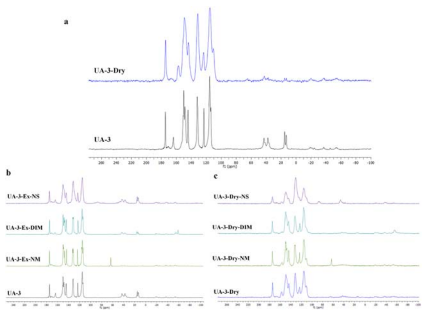

Fig. 10 The solid state ^{13}C-CP/MAS NMR spectrum of (a) UA-3 and UA-3-Dry (b) UA-3-Ex-X and (c) UA-3-Dry-X and their comparison.

crystallinity restoration depends on the type of guest molecule used for resoaking, with NM producing the most significant improvement, followed by DIM, while NS has the least impact.

The ability of UA-3 to reversibly regain crystallinity after guest removal sets it apart from reported urea-MOFs. These features not only enhance functional accessibility but also establish UA-3 as a rare example of a topologically distinct and guest-adaptive urea MOF.

4. Conclusion

In this study, three novel urea-functionalized MOFs: UA-1, UA-2, and UA-3 have been successfully synthesized by varying solvothermal reaction conditions such as solvent, temperature, and concentration of starting material. UA-1 and UA-2 displayed poly-catenated structures with four-fold interpenetration, while UA-3 presented a unique, non-interpenetrating mesoporous structure with hexagonal channels, a novel topology among urea-functionalized MOFs. One of the advantages of UA-3 is the facile preparation, with large channels decorated by six free double –NH groups of the urea functionality, and without employing costly ligands. We also explored the host–guest interactions within UA-3 and different organic molecules using a combination of single-crystal X-ray diffraction, solid state-NMR spectroscopy, and TGA. A comprehensive intermolecular analysis of different organic guest molecules and UA-3 showed preferential assembly of guest molecules at the urea-functionalized sites within the channels. Guest molecules, based on their polarity and functionality preferentially congregated around the freely accessible hydrogen bond donating groups, which we deliberately incorporated into the UA-3 structure to prevent their self-assembly. Full removal of H-bond accepting solvent decreased the crystallinity, possibly due to disorder related to reorientation of the urea groups to find hydrogen bonding partners. This research shows that precisely tailoring pore walls has the potential to influence not only the adsorption but also the orientation of guest molecules. It also highlights how using the right catalytically active groups within a porous platform could effectively control chemical reactions, making them highly promising for catalytic applications. Our results contribute valuable insights into the design and functionality of urea-functionalized MOFs for use across various scientific and industrial contexts.

Data availability

The data supporting this article are included in the ESI.† Crystallographic data: The X-ray crystallographic data for UA-1,2 &3, UA-3-Ex-NM, UA-3-Ex-DIM, UA-3-Ex-N, UA-3-Dry, UA-3-Dry-NM, UA-3-Dry-DIM, UA-3-Dry-NS has been deposited at the CCDC as ESI Data† with deposition number of: 2389779, 2389772, 2389773, 2389776, 2389778, 2389777, 2389774, 2389770, 2389775 and 2389771.

Conflicts of interest

There are no conflicts to declare.

Acknowledgements

Financial support from the Fonds Wetenschappelijk Onderzoek (FWO) under grant number 12E5323N, the Excellence of Science (EOS) project Phospore (ref. 40007504) and the medium-scale research infrastructure project (reference I012324N) is gratefully acknowledged. Crystallographic studies were in part conducted using equipment of and help from the Bruker (Karlsruhe) and Rigaku (Frankfurt) Application Centers. We thank Christian Schürmann and Tobias Stürzer for their kind help. Financial support was also provided by Hasselt University and the Research Foundation Flanders (FWO Vlaanderen) *via* the Hercules project (AUHL/15/2-GOH3816N).

Notes and references

1 W. Zhang, R. Taheri-Ledari, M. Saeidirad, F. S. Qazi, A. Kashtiaray, F. Ganjali, Y. Tian and A. Maleki, *J. Environ. Chem. Eng.*, 2022, **10**, 108836.
2 J. Liu, T. A. Goetjen, Q. Wang, J. G. Knapp, M. C. Wasson, Y. Yang, Z. H. Syed, M. Delferro, J. M. Notestein and O. K. Farha, *Chem. Soc. Rev.*, 2022, **51**, 1045–1097.
3 L. Feng, K.-Y. Wang, J. Willman and H.-C. Zhou, *ACS Cent. Sci.*, 2020, **6**, 359–367.
4 I. Abánades Lázaro, X. Chen, M. Ding, A. Eskandari, D. Fairen-Jimenez, M. Giménez-Marqués, R. Gref, W. Lin, T. Luo and R. S. Forgan, *Nat. Rev. Methods Primers*, 2024, **4**, 42.
5 A. Dhakshinamoorthy, Z. Li and H. Garcia, *Chem. Soc. Rev.*, 2018, **47**, 8134–8172.
6 Z. J. Wang, K. N. Clary, R. G. Bergman, K. N. Raymond and F. D. Toste, *Nat. Chem.*, 2013, **5**, 100–103.
7 P. W. Kenny, *J. Med. Chem.*, 2022, **65**, 14261–14275.
8 L. Zhao, J. Cai, Y. Li, J. Wei and C. Duan, *Nat. Commun.*, 2020, **11**, 2903.
9 L. Chen, B. Zhang, L. Chen, H. Liu, Y. Hu and S. Qiao, *Mater. Adv.*, 2022, **3**, 3680–3708.
10 S. Vera, A. García-Urricelqui, A. Mielgo and M. Oiarbide, *Eur. J. Org Chem.*, 2023, **26**, e202201254.
11 X.-W. Dong, T. Liu, Y.-Z. Hu, X.-Y. Liu and C.-M. Che, *Chem. Commun.*, 2013, **49**, 7681–7683.
12 X.-J. Wang, J. Li, Q.-Y. Li, P.-Z. Li, H. Lu, Q. Lao, R. Ni, Y. Shi and Y. Zhao, *CrystEngComm*, 2015, **17**, 4632–4636.
13 M. Raynal, P. Ballester, A. Vidal-Ferran and P. W. Van Leeuwen, *Chem. Soc. Rev.*, 2014, **43**, 1734–1787.
14 P. Tundo, P. Anastas, D. S. Black, J. Breen, T. J. Collins, S. Memoli, J. Miyamoto, M. Polyakoff and W. Tumas, *Pure Appl. Chem.*, 2000, **72**, 1207–1228.
15 X. Fang and C.-J. Wang, *Chem. Commun.*, 2015, **51**, 1185–1197.
16 V. J. Lillo, J. Mansilla and J. M. Saa, *Angew. Chem.*, 2016, **128**, 4384–4388.
17 J. M. Roberts, B. M. Fini, A. A. Sarjeant, O. K. Farha, J. T. Hupp and K. A. Scheidt, *J. Am. Chem. Soc.*, 2012, **134**, 3334–3337.

18 M. J. Katz, Z. J. Brown, Y. J. Colón, P. W. Siu, K. A. Scheidt, R. Q. Snurr, J. T. Hupp and O. K. Farha, *Chem. Commun.*, 2013, **49**, 9449–9451.
19 J. H. Cavka, S. Jakobsen, U. Olsbye, N. Guillou, C. Lamberti, S. Bordiga and K. P. Lillerud, *J. Am. Chem. Soc.*, 2008, **130**, 13850–13851.
20 C. M. McGuirk, M. J. Katz, C. L. Stern, A. A. Sarjeant, J. T. Hupp, O. K. Farha and C. A. Mirkin, *J. Am. Chem. Soc.*, 2015, **137**, 919–925.
21 A. A. Tehrani, S. Abedi, A. Morsali, J. Wang and P. C. Junk, *J. Mater. Chem. A*, 2015, **3**, 20408–20415.
22 X. Zhang, Z. Chen, X. Liu, S. L. Hanna, X. Wang, R. Taheri-Ledari, A. Maleki, P. Li and O. K. Farha, *Chem. Soc. Rev.*, 2020, **49**, 7406–7427.
23 Z. Chen, K. O. Kirlikovali, P. Li and O. K. Farha, *Acc. Chem. Res.*, 2022, **55**, 579–591.
24 J. Lippke, B. Brosent, T. von Zons, E. Virmani, S. Lilienthal, T. Preuße, M. Hülsmann, A. M. Schneider, S. Wuttke and P. Behrens, *Inorg. Chem.*, 2017, **56**, 748–761.
25 M. M. Deegan, A. M. Antonio, G. A. Taggart and E. D. Bloch, *Coord. Chem. Rev.*, 2021, **430**, 213679.
26 N. Bönisch, M. Maliuta, I. Senkovska, V. Bon, P. Petkov, C. Plätzer, P. Müller and S. Kaskel, *Inorg. Chem.*, 2021, **60**, 1726–1737.
27 H.-L. Jiang, T. A. Makal and H.-C. Zhou, *Coord. Chem. Rev.*, 2013, **257**, 2232–2249.
28 S. Kitagawa, R. Kitaura and S. i. Noro, *Angew. Chem., Int. Ed.*, 2004, **43**, 2334–2375.
29 M. Guo and Z.-M. Sun, *J. Mater. Chem.*, 2012, **22**, 15939–15946.
30 A. Ferguson, L. Liu, S. J. Tapperwijn, D. Perl, F.-X. Coudert, S. Van Cleuvenbergen, T. Verbiest, M. A. Van Der Veen and S. G. Telfer, *Nat. Chem.*, 2016, **8**, 250–257.
31 G. Verma, S. Butikofer, S. Kumar and S. Ma, *Metal-Organic Framework: From Design to Applications*, 2020, pp. 89–133.
32 C. A. Bauer, T. V. Timofeeva, T. B. Settersten, B. D. Patterson, V. H. Liu, B. A. Simmons and M. D. Allendorf, *J. Am. Chem. Soc.*, 2007, **129**, 7136–7144.
33 J. V. Alegre-Requena, E. Marqués-López, R. P. Herrera and D. D. Díaz, *CrystEngComm*, 2016, **18**, 3985–3995.
34 N. Busschaert, C. Caltagirone, W. Van Rossom and P. A. Gale, *Chem. Rev.*, 2015, **115**, 8038–8155.
35 X. Wu, L. K. Macreadie and P. A. Gale, *Coord. Chem. Rev.*, 2021, **432**, 213708.
36 A. Azhdari Tehrani, L. Esrafili, S. Abedi, A. Morsali, L. Carlucci, D. M. Proserpio, J. Wang, P. C. Junk and T. Liu, *Inorg. Chem.*, 2017, **56**, 1446–1454.
37 A. L. Spek, *Acta Crystallogr., Sect. C:Struct. Chem.*, 2015, **71**, 9–18.
38 I. J. Bruno, J. C. Cole, P. R. Edgington, M. Kessler, C. F. Macrae, P. McCabe, J. Pearson and R. Taylor, *Acta Crystallogr., Sect. B:Struct. Sci.*, 2002, **58**, 389–397.
39 M. O'Keeffe and O. M. Yaghi, *Chem. Rev.*, 2012, **112**, 675–702.
40 V. A. Blatov, A. P. Shevchenko and D. M. Proserpio, *Cryst. Growth Des.*, 2014, **14**, 3576–3586.
41 L. Zoubritzky and F.-X. Coudert, *SciPost Chem.*, 2022, **1**, 005.
42 L. T. Glasby, J. L. Cordiner, J. C. Cole and P. Z. Moghadam, *Chem. Mater.*, 2024, **36**, 9013–9030.
43 J. E. Mondloch, W. Bury, D. Fairen-Jimenez, S. Kwon, E. J. DeMarco, M. H. Weston, A. A. Sarjeant, S. T. Nguyen, P. C. Stair and R. Q. Snurr, *J. Am. Chem. Soc.*, 2013, **135**, 10294–10297.
44 Q. Fang, CSD Communication, refcode FUSYUO, deposition number 255509, 2009, DOI: **10.5517/cc8kw7x**.
45 E. V. Alexandrov, A. P. Shevchenko, N. A. Nekrasova and V. A. Blatov, *Russ. Chem. Rev.*, 2022, **91**, RCR5032.
46 J. Li and J. Sun, *Acc. Chem. Res.*, 2017, **50**, 2737–2745.
47 P. Adriaensens, L. Storme, R. Carleer, J. Gelan and F. Du Prez, *Macromolecules*, 2002, **35**, 3965–3970.